

# **Title: Human interictal epileptiform discharges are traveling waves reflecting ictal self-organization**

**Authors:** Elliot H Smith<sup>1,2\*</sup>, Jyun-You Liou<sup>3</sup>, Edward M. Merricks<sup>2</sup>, Tyler S Davis<sup>1</sup>, Kyle Thomson<sup>4</sup>, Bradley Greger<sup>5</sup>, Paul A House<sup>6</sup>, Ronald G Emerson<sup>7</sup>, Robert R Goodman<sup>8</sup>, Guy M McKhann II<sup>9</sup>, Sameer A Sheth<sup>10</sup>, Catherine A Schevon<sup>2</sup>, John D Rolston<sup>1\*</sup>

## **Affiliations:**

<sup>1</sup>Departments of Neurosurgery and Biomedical Engineering, University of Utah, Salt Lake City, UT, USA; 84117.

<sup>2</sup>Department of Neurology, Columbia University, New York, NY, USA; 10032.

<sup>3</sup>Department of Anesthesiology, Weill Cornell Medicine, New York, NY, USA; 10065.

<sup>4</sup>Department of Pharmacology & Toxicology, University of Utah, Salt Lake City, UT; 84117.

<sup>5</sup>Department of Bioengineering, Arizona State University, Tempe, AZ; 85281.

<sup>6</sup>Neurosurgical Associates, LLC, Murray, UT; 84107.

<sup>7</sup>Hospital for Special Surgery, New York, NY, USA; 10021.

<sup>8</sup>Lenox Hill Hospital, New York, NY; 10075

<sup>9</sup>Department of Neurological Surgery, Columbia University, New York, USA; 10032

<sup>10</sup>Department of Neurosurgery, Baylor College of Medicine, Houston, TX, USA; 77030

\*To whom correspondence should be addressed: [john.rolston@hsc.utah.edu](mailto:john.rolston@hsc.utah.edu), [e.h.smith@utah.edu](mailto:e.h.smith@utah.edu)

**One Sentence Summary:** Epileptiform electrical events occurring between human seizures propagate across the brain in directions that reflect the self-organizing structure of seizures.

**Abstract:** Interictal epileptiform discharges (IEDs), also known as interictal spikes, are large intermittent electrophysiological events observed between seizures in patients with epilepsy. While seizures are infrequent and unpredictable, IEDs are far more common, often occurring several times per minute. Yet despite the abundance of IEDs, it remains unknown how they relate to seizures. To better understand this relationship, we examined multi-day recordings of 96-channel microelectrode arrays implanted in human epilepsy patients. These recordings—spanning single cell action potentials to population field potentials—allowed us to study the microscale spatiotemporal organization of over 45,000 IEDs across 10 participants from 2 surgical centers. These recordings showed that the majority of IEDs propagate across neocortex as traveling waves. While all of these traveling wave distributions exhibited a predominant, consistent direction, the majority also exhibited a second, auxiliary, direction. Clustering the IED distributions revealed that their predominant and auxiliary distributions were antipodal, mimicking the spatial microstructure of seizure discharges (SDs) that we have previously reported. We thus compared spatial features of IED sub-distributions to those for SDs, showing a correspondence between ictal and interictal spatial properties in participants whose microelectrode arrays were recruited into the seizure from adjacent cortical tissue. These results reveal fundamental relationships between IEDs and seizures and suggest how IEDs could be used to infer spatial features of seizures.

## Introduction

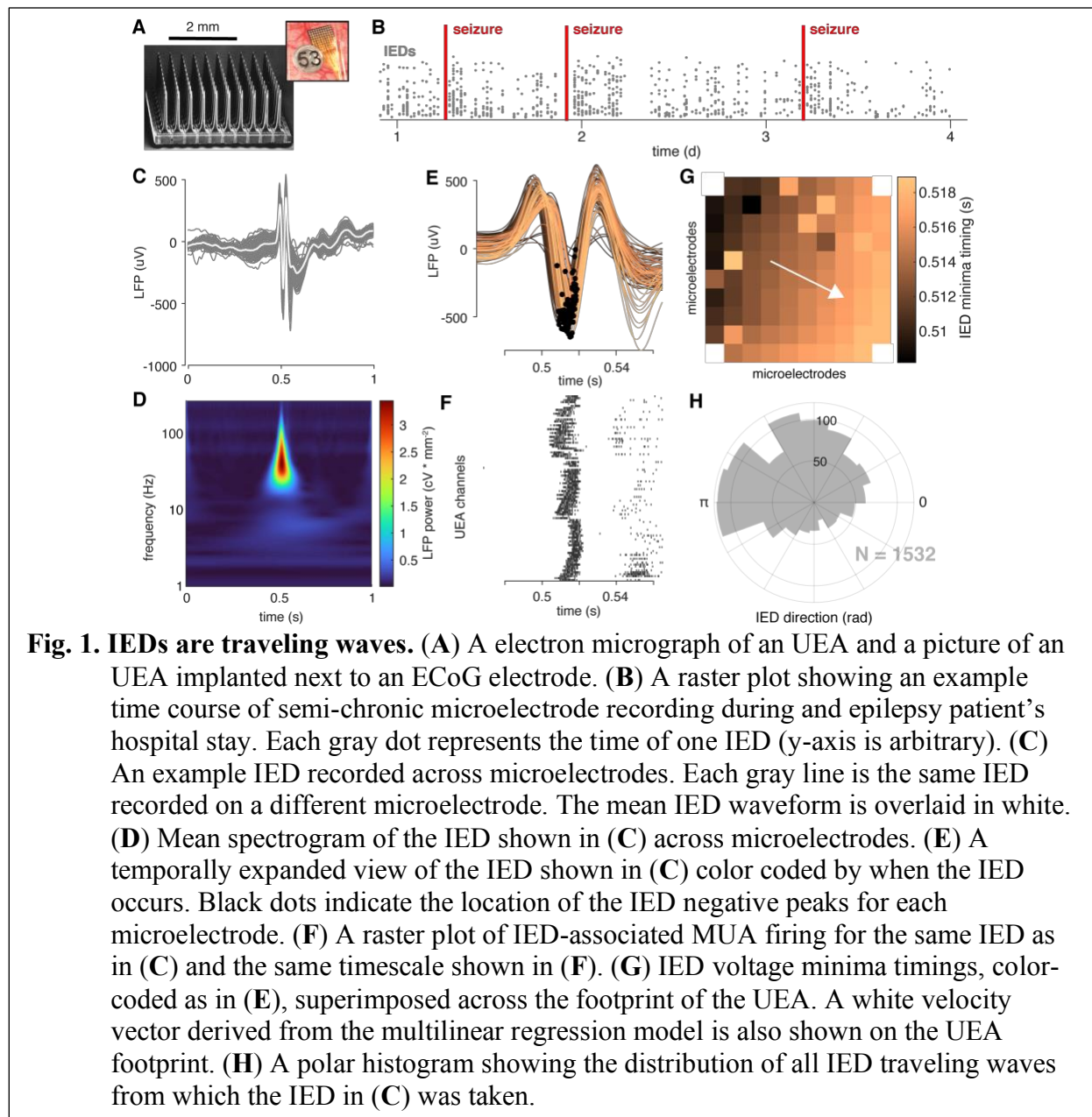
While seizures are mostly unpredictable and rare, electrical recordings from people with epilepsy often show isolated epileptiform discharges between seizures (1–4). These IEDs are far more frequent, occurring up to several times per minute, and exhibit multidien variation in their frequency that correlates with seizure likelihood, making IEDs an attractive personalized biomarker for seizure risk (5). Intracranial recordings in epilepsy patients have shown evidence for some overlap between cortical areas with more IEDs and the areas where seizures originate, though IEDs are more widely distributed (4, 6, 7). Furthermore, some retrospective studies showed that removing brain areas with more IEDs was associated with improved surgical outcomes in patients with medically refractory epilepsy (8, 9). Despite these findings, the long-debated relationship between IEDs and seizure generating tissue remains unresolved (2, 10–12). A functional explanation of the relationship between IEDs and seizures will inform how IEDs can be used to improve the diagnosis and treatment of medically refractory epilepsy.

Microelectrode array recordings in epilepsy patients, which sample the activity of both individual neurons and field potentials, have revealed the spatiotemporal features of ictal self-organization (13–17). These studies reported two classes of recordings, those in which neuronal firing is recruited into the ongoing seizure, and those in which neuronal firing is relatively unaffected, despite seizure-like field potentials appearing on the same microelectrodes. These classes correspond to two dynamically evolving regions known as the ictal *core* and *penumbra*, respectively (15). A slowly-propagating, narrow band of tonic action potential firing, the ictal wavefront (IW), delineates the transition between the core and penumbra (18, 19). These dynamic seizure regions also exhibit distinct spatial features. The slowly traveling IW repetitively emits rapidly traveling SDs (also known as ictal discharges) toward the seizure core. Though, in some patients, SDs are also emitted outwards, towards the penumbra (14).

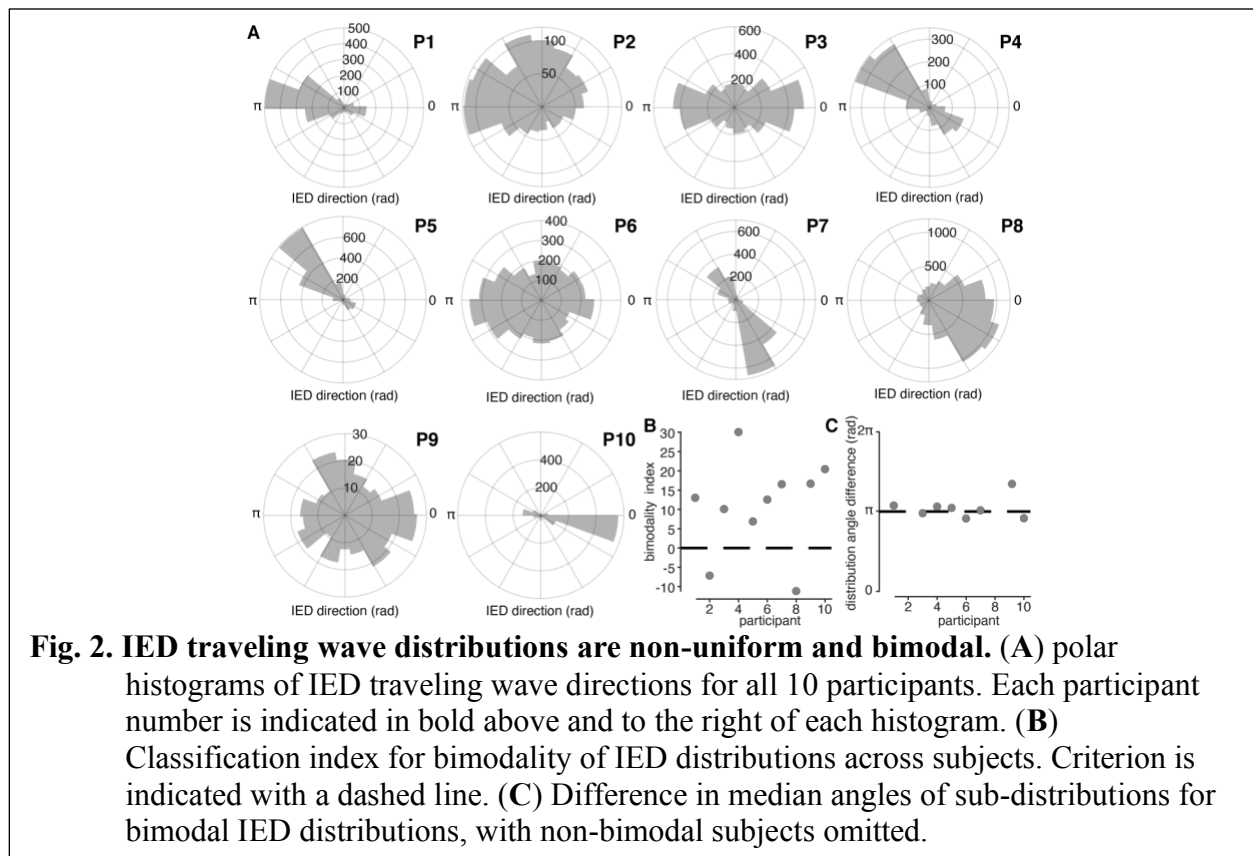
Here we use similar microelectrode array recordings to understand how spatial features of IEDs relate to spatial features of seizures. This study was motivated by our recent theoretical model inspired by the aforementioned spatial dynamics of ictal self-organization discovered from microelectrode array recordings (21). One prediction of the model is that the repeated barrages of traveling synaptic activity during SDs eventually coopt mechanisms of synaptic plasticity, biasing local tissue to propagate IEDs in similar directions as SDs. We sought to empirically validate the model prediction that IEDs are traveling waves that are biased in the same directions as ictal discharges. This question is most relevant for microelectrode recordings in which both seizure expansion (i.e. IW expansion) and SD propagation could be measured. We hypothesized that IEDs have a predominant direction of propagation, towards the site of seizure onset, and antipodal to the direction of seizure expansion. The data supported this hypothesis, and further showed that, in the majority of participants, IEDs traveled bimodally on a linear axis with spatial features of IEDs echoing spatial features of SDs.

## Results

### *Participants, data collection, and IED detection*



Hypotheses were addressed via analysis of a multi-institutional dataset of Utah-style microelectrode array (UEA; 10 X 10 microelectrodes in 4 X 4 mm grid, penetrating 1 mm) recordings from 10 epilepsy patients (2 female,  $\mu \pm \sigma$  age:  $29 \pm 5.24$  years) undergoing monitoring for neurosurgical treatment of their medically refractory epilepsy (clinical details in Extended Table 1). In order to capture seizures ( $2.2 \pm 1.6$  seizures recorded per participant; 22 total), we recorded data continuously throughout the patients' monitoring periods (Figure 1A;  $4.3 \pm 2.4$  days per participant; 43 total). Searching through weeks' worth of microelectrode data, we detected 45,623 candidate IEDs across the 10 participants ( $4,562.3 \pm 5,171.7$  per participant) using an IED detection algorithm designed for microelectrode recordings, that operated on features of IEDs based on the American Clinical Neurophysiological Society's definition, namely high-amplitude bursts of beta-range (20-40 Hz) local field potential (LFP) power occurring across multiple microelectrodes (Fig. S1; Algorithm S1) (1). Using this algorithm, we



detected an average of  $0.43 \pm 0.51$  IEDs per minute. The UEA enabled us to record both LFP data and multiunit action potential firing (MUA) across high-density spatial grid during each IED. These features of an example IED are shown in Figure 1C-G.

### *IEDs propagate in predominant and auxiliary directions*

In order to determine whether the detected IEDs were traveling waves, and to measure wave speeds and directions, we fit a plane to the timings of both IED voltage extrema and MUA event times measured on each microelectrode using multi-linear regression (20). IEDs with regression slopes that were significantly different from zero were classified as traveling waves (permutation test against a distribution of 1000 spatially permuted timings; Fig. 1H, Fig. S2). Traveling wave speeds and directions were then derived from each significant model's slope. Based on this operational definition, 30,278 IEDs ( $3,027.8 \pm 3,190.0$  per participant) were classified as traveling waves (66.4%).

Summary statistics for the spatiotemporal features of IEDs are shown in Table 1. IED speeds were on the same order as SDs before the passage of the ictal wavefront (14, 20). Traveling waves were also detected from MUA, independent of LFP recordings, though at a slightly reduced rate ( $2,215.7 \pm 3,237.6$  per participant; 22,157 total; 48.6%;  $\chi^2 = 2957$ ,  $p < 0.05$ ). This result was expected, as LFP is a more reliable signal to record, and action potential firing during IEDs has previously been shown to be remarkably heterogeneous, particularly in areas further from the seizure onset zone (22). That there were significantly more IED traveling waves in UEA recordings that were eventually recruited into the seizure core, further supports the idea that more firing, closer to the seizure onset zone improves reliability of traveling wave

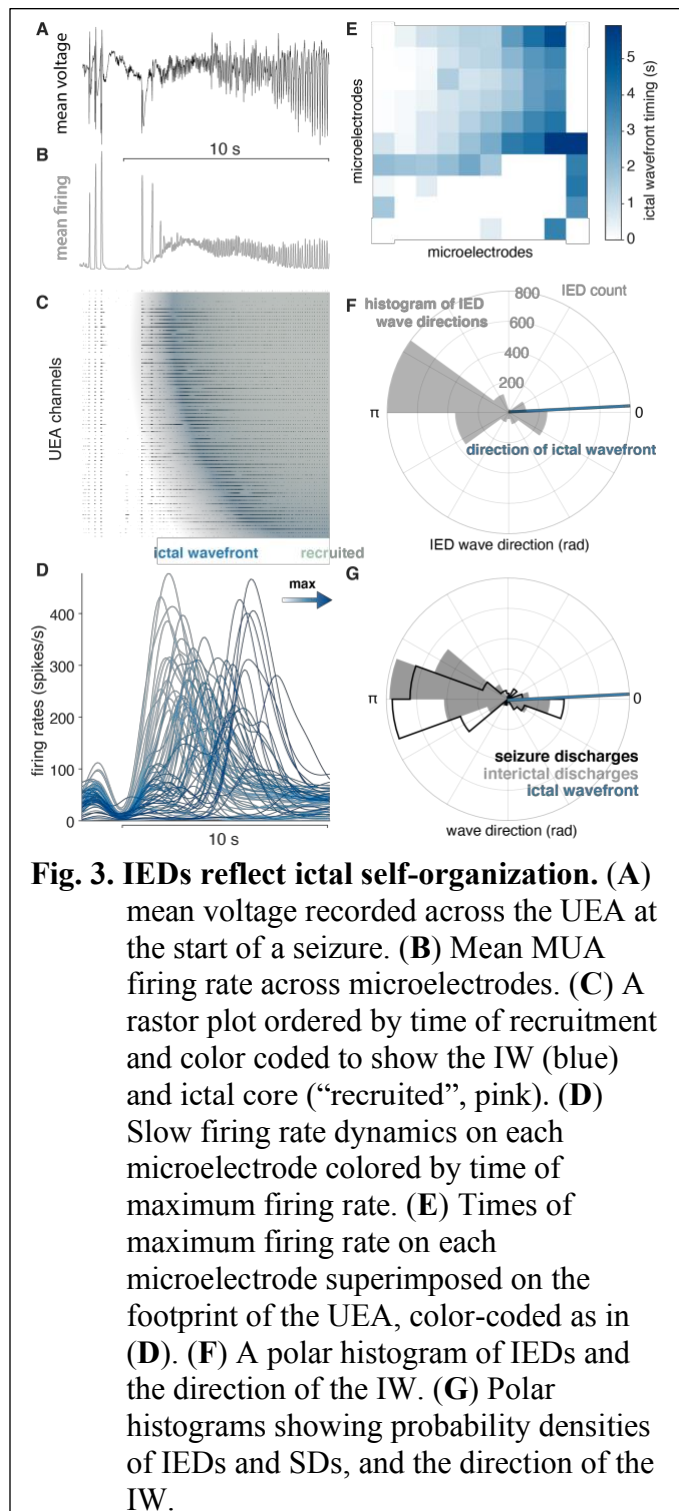
detection with MUA (McNemar Test,  $\chi^2(1) = 2957$ ,  $p < 10^{-6}$ ). We therefore focus our analysis on IED traveling waves measured from LFP minima in order to understand IED propagation across participants.

Having determined the majority of IEDs met the criteria to be classified as traveling waves, we next sought to understand whether IEDs from each participant exhibited a predominant propagation direction. We therefore tested whether distributions of IED traveling wave directions deviated from a uniform circular distribution (23), we found that each participant's IED traveling wave distribution exhibited a dominant direction (Fig. 2A; Hermans-Rasson Tests, 1000 permutations, all  $p < 10^{-3}$ ). These results show that many IEDs are traveling waves with predominant, consistent directions of travel in each participant.

In addition to a predominant direction common to all participants, many participants appeared to have a second, auxiliary, distribution of IED directions. We therefore fit each participant's IED distribution into a mixture of two circular normal sub-distributions (von Mises distribution). The mixture model was compared to a single von Mises distribution model by using permutation-based Kuiper tests (see **Materials and Methods**). IED traveling wave distributions were thus classified as bimodal in 8 of the 10 participants (Figure 2B). The mean and s.d. angles between the two IED sub-distributions was 177.9 and 10.7 degrees, respectively (Figure 2C). These results show that IEDs also frequently propagate antipodally to their predominant direction, suggesting that IEDs may travel both directions on a linear track through a fixed recording site.

### *Spatial features of IED distributions reflect ictal self-organization*

We next sought to understand whether IED speed and direction related to the spatial self-organization of seizures.



We hypothesize that spatial features of IED traveling waves would correlate with seizure propagation direction and those of seizure discharges. We therefore measured the spatial features of seizures first. Fast and slow spatial features of focal seizures were measured in both ictal LFP and MUA bands as in previous reports (14, 15, 20). Both of these features were measured using the same multilinear regression framework used to measure IED speed and direction.

Following previous reports with microelectrode arrays, we confirmed that seizures could be divided into two classes based on ictal recruitment: “recruited” and “penumbral” (see **Materials and Methods**; 14, 24, 25). Recruited tissue exhibited a slow expansion of tonic neuronal firing, the ictal wavefront (Fig. 3D-E; Fig. S4A-D), followed by rapidly traveling SDs (Movie S1). Penumbral tissue showed neither an IW nor repetitive SDs associated with phase-locked firing (Fig. S4E-H). Six participants’ microelectrode arrays were recruited into the ictal core (10 seizures; Fig. 3A-C), while the four remaining participants were penumbral (12 seizures, Fig. S4E-H).

As predicted by our theoretical work (21), similar patterns of IED and SD propagation were apparent in the majority of seizures in participants with “recruited” seizures. The majority of IEDs travelled opposite the direction of seizure expansion (i.e., the IW; direction difference from IEDs =  $148.9 \pm 17.2$  degrees; median tests between IW and IED distributions, all  $p < 0.05$ ; Fig. 3F). Moreover, IEDs traveled in similar directions as SDs in these participants (example in Fig. 3G; mean  $\pm$  s.d. angle difference across participants =  $23.7 \pm 33.7$  degrees). Direction distributions for IEDs, SDs, relative to the direction of the ictal wavefront are shown for all “recruited” participants in Figures 4A-F, and direction summaries for these participants are shown in Figures 4G-H (raw directions shown in Fig. S5). In the “penumbral” category, where the tissue under the UEAs were not obviously recruited from adjacent cortex as in the “recruited” category, we could not reliably detect or measure the direction of seizure expansion.

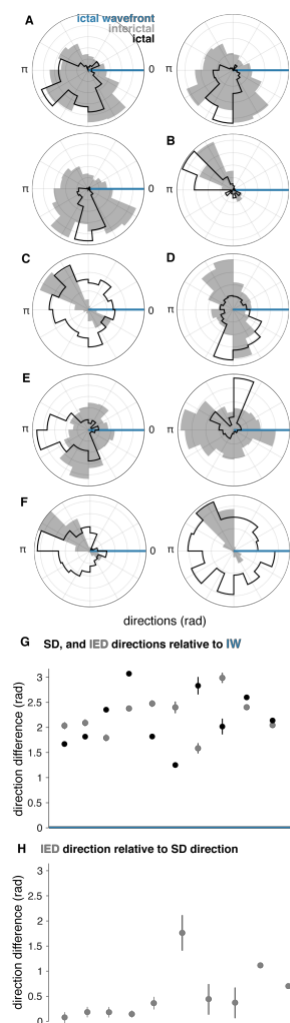


**Fig. 4. IED and SD distributions in “recruited” UEA recordings.** (A-F) Each lettered subpanel corresponds to one participant. Each polar histogram corresponds to one seizure. IED distributions are shown in gray and SD distributions are shown in black. Each distribution is plotted relative to the direction of the IW (blue line). (G) Direction difference summaries for each seizure ordered and color coded as in (A-F). Dots indicate median directions and lines indicate standard deviations. (H) Median and standard deviation IED direction summaries relative to median SD directions.

# *Only spatial features of IED sub-distributions correspond to SD sub-distributions*

Finally, we sought to further understand geometric features of bimodal IED distributions and how they related to patterns of SD propagation. Such an understanding was only relevant for the “recruited” participants with bimodal IED distributions (5 participants, 7 seizures). Using the same bimodality classification strategy as for IEDs, we found that 5 of the 7 these seizures in these participants exhibited bimodal SD distributions, with similarly antipodal sub-distribution directions (Fig. 5A-B; mean  $\pm$  s.d. angle difference =  $135.2 \pm 24.6$ ). Only participants with bimodal IED distributions had bimodal SD distributions, and only one participant, who had the least bimodal IED distribution, did not have clearly bimodal SDs.

In order to determine whether IEDs in each sub-distribution came from neurophysiologically distinct IED populations, we tested for differences between IED waveforms and firing rates between IED sub-distributions. Such differences might indicate that each IED sub-distribution reflected a separate population of IEDs propagating across the footprint of the UEA. However, neither firing rates nor IED waveforms differed between IED sub-distributions (Fig. 5C-D; cluster-based permutation tests, all  $p > 0.05$ ), indicating that neither IED waveforms nor firing rates between the two sub-distributions could be statistically distinguished.

The aforementioned results indicate that both SDs and IEDs propagate antipodally through the same tissue. Differences between speeds and proportions of IED sub-distributions, corresponding to those we previously showed in SD sub-distributions (14), would support a learned relationship between IEDs and SDs, as predicted by the centripetal pattern of learning in the theoretical model (21). To address this question, we tested for differences in speed and relative size of SD and IED sub-distributions. Speeds were significantly different between IED sub-distributions within each participant (Fig. 5E; Mann-Whitney U, all  $p < 10^{-4}$ ). Speeds were also significant between SD sub-distributions in five of the seven seizures (Fig. 5E; Mann-Whitney U,  $p < 0.04$  in 5 seizures;  $p > 0.62$  in two seizures). Finally, the proportion of IED directions in each sub-distribution predicted the direction of each SD sub-distribution in four of the five participants (two sample proportion tests,  $\chi^2 > 347.6$ ,  $p < 10^{-6}$ ). More pre-recruitment discharges occurred in a fifth patient with nearly equivalent proportions of IEDs across sub-distributions. Importantly the directions of significant differences in these spatial features corresponded across IED and SD sub-distributions. These results show that when IED and SD distributions were bimodal, their spatial features were similar, underscoring the extent to which IEDs mimic spatiotemporal features of ictal self-organization.

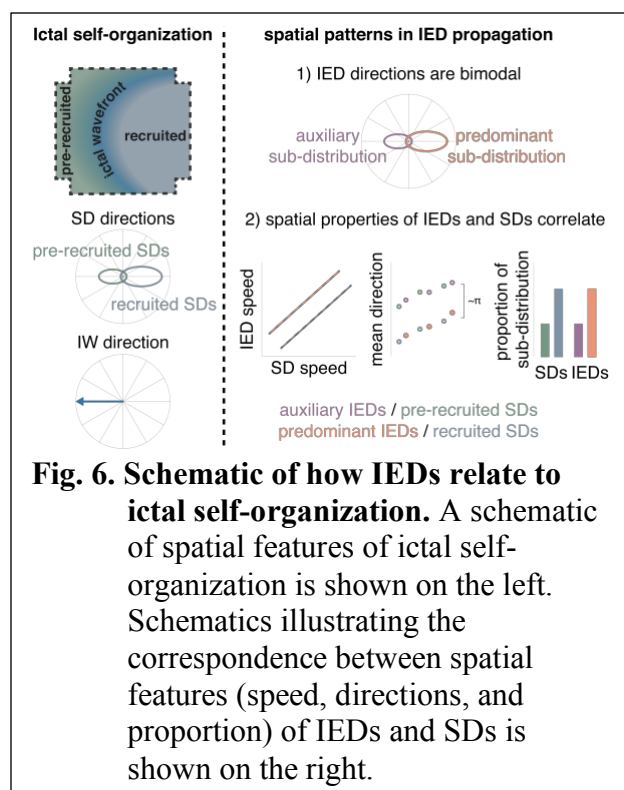
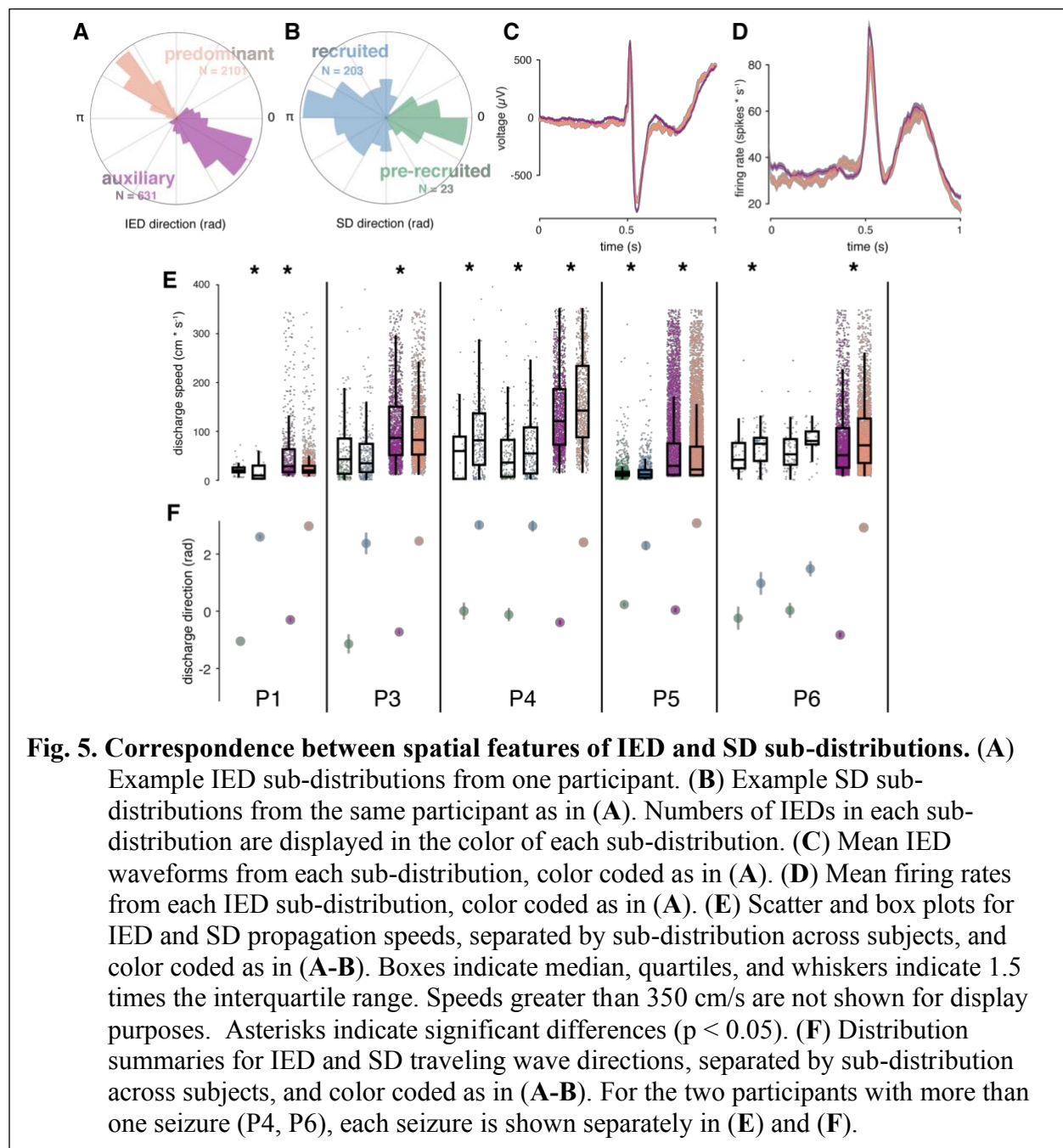


**Fig. 6. Schematic of how IEDs relate to ictal self-organization.** A schematic of spatial features of ictal self-organization is shown on the left. Schematics illustrating the correspondence between spatial features (speed, directions, and proportion) of IEDs and SDs is shown on the right.



## Discussion

Our results, using microelectrode array recordings in patients with epilepsy, show that IEDs are traveling waves that propagate in similar directions as SDs, along an axis intersecting the seizure core. This corroborates the predictions of our theoretical work, where a computational model incorporating spike-timing dependent plasticity and realistic connectivity between inhibitory and excitatory cells self-organized to produce IWs, SDs, and IEDs that echo through the pathways potentiated by the strong, repeated barrages of SD activity, antipodal to the IW (21, 26). Therefore these results suggest that the predominant IED direction could be used to

localize the seizure source. Moreover, the empirical results reported here extend our understanding of the geometric properties of epileptic tissue, beyond the model predictions, in showing that IEDs travel largely bidirectionally on a linear axis. The bidirectional propagation of IEDs is similar to the bidirectional traveling waves we have previously observed during seizures (14, 20). The bidirectional pattern of traveling waves during seizures emanated from a slowly expanding, motile source of ictal activity—the IW—passing through a fixed recording site (14). The data presented here show that IEDs travel in similarly oriented, bimodal distributions, even in the absence of an IW or ictal self-organization (Fig. 6).

The theoretical model predicted that the directional preferences of IEDs were learned from SDs via spike-timing dependent plasticity (27). While we cannot address the specific learning mechanism with this dataset, in participants whose UEAs were recruited into the seizure core from adjacent cortical tissue, we showed correspondences between several spatial properties of IEDs and SDs. The speeds, directions, and relative sizes of IED sub-distributions echoed those of SDs. Moreover, predominant IED and SD directions opposed the directions of the ictal wavefronts in “recruited” UEAs. These relationships were unable to be determined from UEAs that were not recruited into the seizure core (“penumbral” recordings). Together, these results suggest that spatiotemporal biases exist in epileptic tissue. Whether spatiotemporal biases in IEDs arise from learning during SDs or vice versa remains to be determined. While the theoretical model indicates that several seizures must occur before IEDs begin to form, electrographic discharges, similar to IEDs, often appear before seizures in animal models of epilepsy (28).

While we show that the majority of IEDs are traveling waves whose directions overlap with those of SDs, it is important to recognize the small spatial scale of the recordings analyzed here. Additional, more eccentric populations of IEDs could be propagating from distant areas that are connected to the seizure onset zone, though not necessarily from adjacent tissue on the cortical surface (29). Higher density ECoG that spans a larger cortical territory than the UEA would be useful in gaining more context on where IEDs arise, and how IEDs propagate across the cortical surface. On the other hand, there is currently no evidence that the ictal wavefront can be detected without action potential recordings, though the time of seizure recruitment can be roughly estimated on each ECoG electrode from high-frequency LFP (25, 30). Precise IED propagation patterns are also difficult to measure with the relatively low sampling density of ECoG. Animal studies using calcium indicators capable of imaging neuronal activity across large cortical territories may overcome these limitations (31, 32). Such animal studies are also poised to understand how learning and plasticity contributes to the geometric relationships reported here.

While these microelectrode array recordings inform fundamental geometric relationships between IED propagation and ictal self-organization, additional spatial context may inform our understanding of “penumbral” tissue (30). Future work will therefore focus on translating these microelectrode array results to a more clinically relevant spatial scale. For example, using ECoG (33, 34) with vector field or convolutional methods (35), or examining propagation of source-localized IEDs in stereo-EEG. Such approaches will be useful for linking the micro results reported in this paper to the coarser spatial resolutions and broader coverages encountered with typical intracranial recordings. Integrating these multi-scale geometrical understandings of how IEDs relate to the seizure onset zone could then provide an additional piece of information to inform diagnosis and treatment of medically refractory epilepsy, and potentially enable localizing the seizure source without having to directly observe seizures.

## Materials and Methods

### *Participants, Ethics Statement, and Data Acquisition*

The data for this study were acquired from Utah-style microelectrode arrays (UEAs) that were implanted in 10 human patients across two surgical sites who were undergoing neurophysiological monitoring for surgical treatment for medically refractory seizures. Clinical details for all participants are shown in Extended Table 1. The Institutional Review Boards at the University of Utah (IRB\_00114691) and Columbia University Medical Center (IRB-AAAB6324) approved these studies. All participants provided informed consent prior to surgery for implantation of the clinical electrocorticography (ECoG) electrodes and UEA (10 x 10 electrodes in 4 x 4 mm, penetrating 1 mm). Methodological details of surgical implantation of UEAs into human epilepsy patients area described in detail in House et al. (36). During implantation of ECoG electrodes, UEAs were pneumatically inserted into areas that were most likely to be in the seizure onset zone, and therefore most likely to be resected. Electrophysiological data were pseudodifferentially amplified by 10 and acquired at 30 kilosamples per second using a neural signal processing system (Blackrock Microsystems, Salt Lake City, UT) semi-chronically, that is throughout the duration of the participants' hospital stays. Throughout the manuscript, numerical quantities are presented as mean  $\pm$  standard deviation (s.d.).

### *IED Detection and signal processing*

In order to detect IEDs from continuous data recorded on each UEA channel, we developed a simple algorithm for detecting IEDs across a microelectrode array (Algorithm S1). For each channel on each UEA, we first resampled the data at 400 samples per second and zero-phase filtered the data between 20 and 40 Hz using a 4<sup>th</sup> order Butterworth filter. We then detected any peaks in the absolute amplitude of this signal that were greater than 8 times the standard deviation of the remainder of the recording segment (2-hour median duration; Fig. S1A). In order to remove redundant detections, those following any other detection by less than 250 ms were discarded. Only detections that occurred within the same 250 ms window across at least 10 electrodes on the UEA were retained for further analysis (Fig. S1B).

Multiunit action potentials (MUA) were detected on each microelectrode by filtering each channel between 0.3 and 3 kilohertz and detecting peaks in the filtered signal less than -4 times its root mean square. The times of these peaks were retained for further analysis. Example retained detections are shown in Fig. S1C-E.

We employed several post-detection processing steps to ensure the quality of this expansive data set, and reject artifacts. First, temporally outlying voltage extrema were removed in order to constrain extrema detection into a temporally focused window (approximately 50 millisecond duration) around the time of IED detection and to exclude broken microelectrodes or those without IED signal. Next, we excluded any discharges with outlying amplitudes, defined as double the interquartile range of the distribution of IED voltage ranges (Fig. S1F-G).

### *Traveling Wave Measurement*

In order to measure IED traveling wave speed and direction, we fit a plane to the timings of IED voltage minima, and MUA event times, using ordinary multilinear regression, regularized via the absolute deviation of the signal (Fig. S2). This methodology is described in detail and validated for measuring traveling waves during ictal discharges in Liou et al. (20). Briefly, the regression model for each IED yielded three coefficients, describing the best-fit plane to the timing of IEDs across the UEA in spacetime. Traveling wave direction was determined by the gradient direction of the plane and speed was defined as the inverse of that gradient norm. Each IED was operationally defined as a traveling wave if its model significantly deviated from a plane with zero slope. Statistical significance for this measure was determined by a permutation test in which the model was reevaluated 1000 times with the microelectrode spatial locations randomly permuted. Differences in IED speed across and within participants were tested using a two-way Kruskal-Wallis Test with a participant factor (10 levels; one for each participant) and a signal factor in which the two levels were the speed measurements derived from LFP and MUA. Only MUA times from 50 ms before and after the median time of the LFP negative peak were included in the regression model (20). Post-hoc pairwise comparisons were carried out using Dunn's test (37). The significance criterion was chosen as 0.05 for all of these tests.

### *Directional Statistics*

Polar histograms were plotted using 18 bins. Circular normal distributions were fit using the circular statistics toolbox (38). These distributions defined by two parameters,  $\mu$  and  $\kappa$ , which describe the central angle and concentration of the distribution, respectively.  $\mu$  and  $1/\kappa$  are analogous to the mean and variance parameters that define a standard normal distribution. Directional statistics were carried out using modified functions from the circular statistics toolbox (38). These modifications were such that statistical significance was evaluated using permutation tests from which p-values were derived by comparing the circular test statistic with a distribution of circular test statistics from 1000 permuted datasets. As an example, testing for differences between IED and SD means would involve comparing the test statistic from the true data to a distribution of 1000 test statistics in which the measurement categories were permuted. The significance criterion was chosen to be 0.05. Hypotheses that within-participant IED propagation directions were non-uniform, were tested with Hermans-Rasson tests of circular non-uniformity, again with 1000 permutations (39).

### *Assessing bimodality and clustering IED sub-distributions*

In order to determine whether two, unimodal distributions better fit the ostensibly bimodal IED and SD distributions we observed, we first fit von Mises Mixture (vMM) Models to overall distributions of IED and SD directions using the Matlab function *fitmvmdist* (<https://github.com/chrschy/mvmdist>). Overall IED direction distributions were then clustered into two component vMM distributions using the Matlab function *cluster*. We did not observe distributions that appeared to have more than two modes and therefore set an upper limit on the number of hypothesized clusters,  $h$ , at two. These vMMs yielded three parameters for each sub-distribution,  $h \in \mathbb{N}$ , such that  $h \leq 2$ : the sub-distribution means,  $\mu_h$ , concentration parameters,  $\kappa_h$ , and probability densities,  $\theta_h$ .

Rather than assuming these vMM models better fit overall IED and SD distributions, we assessed whether the overall distribution or each vMM sub-distribution better fit the distributions

defined by  $\mu_h$  and  $\kappa_h$ . The permutation-based Kuiper tests used to assess goodness-of-fit were carried out as follows. We first estimated  $\mu_h$ ,  $\kappa_h$ , and  $\theta_h$  for both the overall and vMM sub-distributions. We then carried out permutation-based Kuiper tests, to compare empirical distributions of 60 randomly sampled IED directions to theoretical circular normal distributions derived from  $\mu_h$  and  $\kappa_h$  from both the original and vMM sub-distributions. We repeated this procedure 1000 times in order to create a permutation distribution. In this way, we were able to measure the extent to which randomly sampled IED angles deviated from theoretical circular distributions defined by the overall and vMM parameters. This is akin to cross-validating vM parameters and choosing  $h$  corresponding to the highest log-likelihood, yet in a model-free way. Comparing Kuiper test statistics to a permutation distribution, rather than zero (the null hypothesis of a uniform distribution), makes the tests more conservative and allows us to determine whether the distribution cannot be determined to be non-normal (40). We then defined our circular bimodality index as the minimum difference between the Kuiper test statistic for the overall distribution and each vMM sub-distribution. Positive bimodality indices thus indicated that overall traveling wave distributions were better modeled as two vMM sub-distributions, and negative bimodality indices indicated that overall traveling distributions were better modeled as a single von Mises distribution. The Matlab functions for implementing these classifications are highlighted in the online code repository.

### *Seizure Characterization*

In order to study the propagation patterns of IEDs relative to seizures, it was necessary to quantify spatial features of SDs and seizure expansion for each recorded seizure. These measures have also been described in previous publications (14, 15, 17, 30). The ictal wavefront is the slowly expanding edge of the seizure representing the spatial signature of failure of feedforward inhibition, and therefore defines recruitment of the tissue surrounding an electrode into the ictal core (24). This biomarker of seizure recruitment and expansion has thus far only been detected with recordings of multiunit firing rates (14), and can also be detected on single microelectrodes by observing widening of action potential waveforms (17, 41). We followed methods from our previous manuscripts to generate multiunit firing rates, i.e. filtering the broadband data between 300 and 3000 Hz and detecting any peaks larger than the median absolute value of the signal divided by 0.6745 (42).

For all seizures, we looked for tonic multiunit firing spreading across the array that would suggest the presence of an ictal wavefront, and phase locked multiunit bursting associated with ictal discharges. We detected the ictal wavefront feature of seizures by smoothing the firing rates on each microelectrode with a 250 millisecond Gaussian kernel and fitting a multilinear regression model to the peaks of these slow firing rate estimates across the UEA (14, 20). We detected ictal discharges by detecting peaks in multiunit firing rates, calculated with a 25 millisecond Gaussian kernel, as we have previously (14, 20). We quantified the propagation direction and speed of ictal discharges using the same methods used to determine IED traveling wave speeds and directions, as in Liou et al. (20). IED speeds and directions were measured in a manner that was blinded to each microelectrode array's recruitment classification. We defined the presence of ictal phase-locked firing with a Hermans-Rasson test of circular uniformity on MUA action potential times across microelectrodes relative to the phase of the mean LFP recorded across the UEA, similarly to (15). Using these measures, we operationally defined two patterns of ictal self-organization, based on observed patterns in these fast and slow spatial features of seizures: "recruited" seizures

were operationally defined as those with a significant ictal wavefront multilinear regression model and significant phase-locked multiunit firing (Fig. S4A-D). “Penumbral” seizures were operationally defined as those seizures in which we were unable to detect an ictal wavefront on the microelectrode array (Fig. S4E-H). Similar classifications of adjacent and non-adjacent recruitment have been reported by other groups (24, 43). For seizures that were associated with secondary generalization, we only included discharges up to the clinically defined point of secondary generalization in order to constrain our study to the dynamics of focal seizure onset and spread.

### *Comparing IED and SD sub-distributions*

For distributions that were determined to be bimodal, we used cluster-based permutation tests to test for differences between median IED waveforms and firing rates between IEDs from the two component vMM distributions for each participant. Mean firing rates were estimated by binning MUA event times into one-hundred 10-ms bins across microelectrodes. In order to test for different directions of overall distributions and sub-distributions of IEDs and SDs, we used Watson-Williams multi-sample tests for equal means. To test for differences in IED speed between different sub-distributions, we used within-participant Mann-Whitney U tests. In order to test differences in the proportion of IEDs from predominant and auxiliary sub-distributions we used two-sample proportion tests. We employed a significance criterion of 0.05 for all of these tests.

### **Supplementary Materials**

Fig. S1. IED detection and artifact rejection.

Fig. S2. Classifying IED traveling waves.

Fig. S3. Procedures for clustering and evaluating the goodness-of-fit of overall and VonMises mixture distributions.

Fig. S4. Examples of each class of microelectrode seizure recording.

Fig. S5. Raw IED and SD distributions in “recruited” UEA recordings.

Table S1. Clinical details for research participants.

Algorithm S1. IED detection with microelectrode array data.

Movie S1. Video of IEDs and ictal recruitment.

### **References:**

1. W. O. Tatum, O. Selioutski, J. G. Ochoa, H. M. Clary, J. Cheek, F. W. Drislane, T. N. Tsuchida, American Clinical Neurophysiology Society Guideline 7: Guidelines for EEG Reporting, *The Neurodiagnostic Journal* **56**, 285–293 (2016).
2. M. de Curtis, J. G. R. Jefferys, M. Avoli, in *Jasper’s Basic Mechanisms of the Epilepsies*, J. Noebels, M. Avoli, M. Rogawski, R. Olsen, A. Delgado-Escueta, Eds. (Oxford University Press, 2012), pp. 213–227.
3. J. Pillai, M. R. Sperling, Interictal EEG and the Diagnosis of Epilepsy, *Epilepsia* **47**, 14–22.

4. G. Alarcon, Origin and propagation of interictal discharges in the acute electrocorticogram. Implications for pathophysiology and surgical treatment of temporal lobe epilepsy, *Brain* **120**, 2259–2282 (1997).
5. M. O. Baud, J. K. Kleen, E. A. Mirro, J. C. Andrechak, D. King-Stephens, E. F. Chang, V. R. Rao, Multi-day rhythms modulate seizure risk in epilepsy, *Nat Commun* **9**, 88 (2018).
6. E. C. Conrad, S. B. Tomlinson, J. N. Wong, K. F. Oechsel, R. T. Shinohara, B. Litt, K. A. Davis, E. D. Marsh, Spatial distribution of interictal spikes fluctuates over time and localizes seizure onset, *Brain* **143**, 554–569 (2020).
7. E. D. Marsh, B. Peltzer, M. W. Brown, C. Wusthoff, P. B. Storm, B. Litt, B. E. Porter, Interictal EEG spikes identify the region of seizure onset in some, but not all pediatric epilepsy patients, *Epilepsia* **51**, 592–601 (2010).
8. O. Smart, D. Maus, E. Marsh, D. Dlugos, B. Litt, K. Meador, Mapping and mining interictal pathological gamma (30–100Hz) oscillations with clinical intracranial EEG in patients with epilepsy, *Expert Systems with Applications* **39**, 7355–7370 (2012).
9. D. W. Kim, H. K. Kim, S. K. Lee, K. Chu, C. K. Chung, Extent of neocortical resection and surgical outcome of epilepsy: Intracranial EEG analysis, *Epilepsia* **51**, 1010–1017 (2010).
10. J. M. Paolicchi, P. Jayakar, P. Dean, I. Yaylali, G. Morrison, A. Prats, T. Resnik, L. Alvarez, M. Duchowny, Predictors of outcome in pediatric epilepsy surgery, *Neurology* **54**, 642–642 (2000).
11. V. N. Vakharia, J. S. Duncan, J.-A. Witt, C. E. Elger, R. Staba, J. Engel, Getting the best outcomes from epilepsy surgery, *Annals of Neurology* **83**, 676–690 (2018).
12. C. Tonini, E. Beghi, A. T. Berg, G. Bogliun, L. Giordano, R. W. Newton, A. Tetto, E. Vitelli, D. Vitezic, S. Wiebe, Predictors of epilepsy surgery outcome: a meta-analysis, *Epilepsy Research* **62**, 75–87 (2004).
13. L.-E. Martinet, G. Fiddymment, J. R. Madsen, E. N. Eskandar, W. Truccolo, U. T. Eden, S. S. Cash, M. A. Kramer, Human seizures couple across spatial scales through travelling wave dynamics, *Nature Communications* **8**, 14896 (2017).
14. E. H. Smith, J. Liou, T. S. Davis, E. M. Merricks, S. S. Kellis, S. A. Weiss, B. Greger, P. A. House, G. M. McKhann II, R. R. Goodman, R. G. Emerson, L. M. Bateman, A. J. Trevelyan, C. A. Schevon, The ictal wavefront is the spatiotemporal source of discharges during spontaneous human seizures, *Nature Communications* **7**, 11098 (2016).
15. C. A. Schevon, S. A. Weiss, G. McKhann, R. R. Goodman, R. Yuste, R. G. Emerson, A. J. Trevelyan, Evidence of an inhibitory restraint of seizure activity in humans, *Nat Commun* **3**, 1060 (2012).
16. T. L. Eissa, K. Dijkstra, C. Brune, R. G. Emerson, M. J. A. M. van Putten, R. R. Goodman, G. M. McKhann, C. A. Schevon, W. van Drongelen, S. A. van Gils, Cross-scale effects of neural

interactions during human neocortical seizure activity, *Proceedings of the National Academy of Sciences* **114**, 10761–10766 (2017).

17. E. M. Merricks, E. H. Smith, R. G. Emerson, L. M. Bateman, G. M. McKhann, R. R. Goodman, S. A. Sheth, B. Greger, P. A. House, A. J. Trevelyan, C. A. Schevon, Neuronal firing and waveform alterations through ictal recruitment in humans, *J. Neurosci.* (2020), doi:10.1523/JNEUROSCI.0417-20.2020.

18. A. J. Trevelyan, D. Sussillo, R. Yuste, Feedforward Inhibition Contributes to the Control of Epileptiform Propagation Speed, *Journal of Neuroscience* **27**, 3383–3387 (2007).

19. A. J. Trevelyan, D. Sussillo, B. O. Watson, R. Yuste, Modular Propagation of Epileptiform Activity: Evidence for an Inhibitory Veto in Neocortex, *Journal of Neuroscience* **26**, 12447–12455 (2006).

20. J. Liou, E. H. Smith, L. M. Bateman, G. M. McKhann, R. R. Goodman, B. Greger, T. S. Davis, S. S. Kellis, P. A. House, C. A. Schevon, Multivariate regression methods for estimating velocity of ictal discharges from human microelectrode recordings, *Journal of Neural Engineering* **14**, 044001 (2017).

21. J. Liou, E. H. Smith, L. M. Bateman, S. L. Bruce, G. M. McKhann, R. R. Goodman, R. G. Emerson, C. A. Schevon, L. Abbott, R. L. Calabrese, J.-M. Ramirez, J.-M. Ramirez, K. Staley, A. Khambhati, Eds. A model for focal seizure onset, propagation, evolution, and progression, *eLife* **9**, e50927 (2020).

22. C. J. Keller, W. Truccolo, J. T. Gale, E. Eskandar, T. Thesen, C. Carlson, O. Devinsky, R. Kuzniecky, W. K. Doyle, J. R. Madsen, D. L. Schomer, A. D. Mehta, E. N. Brown, L. R. Hochberg, I. Ulbert, E. Halgren, S. S. Cash, Heterogeneous neuronal firing patterns during interictal epileptiform discharges in the human cortex, *Brain* **133**, 1668–1681 (2010).

23. R. Fisher, Dispersion on a Sphere, *Proceedings of the Royal Society A: Mathematical, Physical and Engineering Sciences* **217**, 295–305 (1953).

24. C. A. Schevon, S. A. Weiss, G. McKhann Jr, R. R. Goodman, R. Yuste, R. G. Emerson, A. J. Trevelyan, Evidence of an inhibitory restraint of seizure activity in humans, *Nature Communications* **3**, 1060 (2012).

25. S. A. Weiss, G. P. Banks, G. M. McKhann, R. R. Goodman, R. G. Emerson, A. J. Trevelyan, C. A. Schevon, Ictal high frequency oscillations distinguish two types of seizure territories in humans, *Brain* **136**, 3796–3808 (2013).

26. Q.-A. Nguyen, P. Moolchand, I. Soltesz, Connecting Pathological Cellular Mechanisms to Large-Scale Seizure Structures, *Trends in Neurosciences* **43**, 547–549 (2020).

27. G. Bi, M. Poo, Synaptic Modifications in Cultured Hippocampal Neurons: Dependence on Spike Timing, Synaptic Strength, and Postsynaptic Cell Type, *The Journal of Neuroscience* **18**, 10464–10472 (1998).

28. K. J. Staley, A. White, F. E. Dudek, Interictal spikes: harbingers or causes of epilepsy?, *Neurosci Lett* **497**, 247–250 (2011).
29. J. N. Gelinas, D. Khodagholy, T. Thesen, O. Devinsky, G. Buzsáki, Interictal epileptiform discharges induce hippocampal–cortical coupling in temporal lobe epilepsy, *Nature Medicine* **22**, 641–648 (2016).
30. E. H. Smith, E. M. Merricks, J.-Y. Liou, C. Casadei, L. Melloni, T. Thesen, D. J. Friedman, W. K. Doyle, R. G. Emerson, R. R. Goodman, G. M. McKhann, S. A. Sheth, J. D. Rolston, C. A. Schevon, Dual mechanisms of ictal high frequency oscillations in human rhythmic onset seizures, *Scientific Reports* **10**, 19166 (2020).
31. M. Wenzel, J. P. Hamm, D. S. Peterka, R. Yuste, Reliable and Elastic Propagation of Cortical Seizures In Vivo, *Cell Reports* **19**, 2681–2693 (2017).
32. J.-Y. Liou, E. Baird-Daniel, M. Zhao, A. Daniel, C. A. Schevon, H. Ma, T. H. Schwartz, Burst suppression uncovers rapid widespread alterations in network excitability caused by an acute seizure focus, *Brain* **142**, 3045–3058 (2019).
33. J. Viventi, D.-H. Kim, L. Vigeland, E. S. Frechette, J. A. Blanco, Y.-S. Kim, A. E. Avrin, V. R. Tiruvadi, S.-W. Hwang, A. C. Vanleer, D. F. Wulsin, K. Davis, C. E. Gelber, L. Palmer, J. Van der Spiegel, J. Wu, J. Xiao, Y. Huang, D. Contreras, J. A. Rogers, B. Litt, Flexible, foldable, actively multiplexed, high-density electrode array for mapping brain activity in vivo, *Nature Neuroscience* **14**, 1599–1605 (2011).
34. D. Khodagholy, J. N. Gelinas, T. Thesen, W. Doyle, O. Devinsky, G. G. Malliaras, G. Buzsáki, NeuroGrid: recording action potentials from the surface of the brain, *Nature Neuroscience* **18**, 310 (2014).
35. L. Muller, G. Piantoni, D. Koller, S. S. Cash, E. Halgren, T. J. Sejnowski, Rotating waves during human sleep spindles organize global patterns of activity that repeat precisely through the night, *eLife* **5**, e17267 (2016).
36. P. A. House, J. D. MacDonald, P. A. Tresco, R. A. Normann, Acute microelectrode array implantation into human neocortex: preliminary technique and histological considerations, *Neurosurgical focus* **20**, 1–4 (2006).
37. O. J. Dunn, Multiple Comparisons Using Rank Sums, *Technometrics* **6**, 241–252 (1964).
38. P. Berens, CircStat: A MATLAB Toolbox for Circular Statistics, *J. Stat. Soft.* **31** (2009), doi:10.18637/jss.v031.i10.
39. L. Landler, G. D. Ruxton, E. P. Malkemper, Circular data in biology: advice for effectively implementing statistical procedures, *Behav Ecol Sociobiol* **72** (2018), doi:10.1007/s00265-018-2538-y.
40. A. S. Louter, J. Koerts, On the Kuiper test for normality with mean and variance unknown, *Statistica Neerlandica* **24**, 83–87 (1970).

41. E. M. Merricks, E. H. Smith, G. M. McKhann, R. R. Goodman, L. M. Bateman, R. G. Emerson, C. A. Schevon, A. J. Trevelyan, Single unit action potentials in humans and the effect of seizure activity, *Brain* **138**, 2891–2906 (2015).
42. R. Q. Quiroga, Z. Nadasdy, Y. Ben-Shaul, Unsupervised Spike Detection and Sorting with Wavelets and Superparamagnetic Clustering, *Neural Computation* **16**, 1661–1687 (2004).
43. L.-E. Martinet, O. J. Ahmed, K. Q. Lepage, S. S. Cash, M. A. Kramer, Slow Spatial Recruitment of Neocortex during Secondarily Generalized Seizures and Its Relation to Surgical Outcome, *Journal of Neuroscience* **35**, 9477–9490 (2015).

**Acknowledgments:** Thanks to the Schevon and Rolston labs.

**Funding:** This work was supported by NIH NINDS R21 NS113031 (J.D.R.), NIH NINDS K23 NS114178 (J.D.R.), NIH S10 OD018211 (C.A.S.), NIH R01 NS084142 (C.A.S.), and a Junior Investigator Award from the American Epilepsy Society (E.H.S.).

**Author contributions:** EHS, JYL, CAS, and JDR conceived of the experiments. EHS, EMM, TSD, KT, BG, PH, RGE, RRG, GMM, SAS, and CAS were involved with data collection. EHS, JYL, and EMM analyzed the data. EHS, JYL, and JDR wrote the manuscript. All authors provided edits to the manuscript.

**Competing interests:** The University of Utah has a financial interest in the company that makes the Utah microelectrode array. Dr. Rolston reports personal fees from Medtronic. Dr. McKhann reports personal fees from Koh Young Inc.

**Data and materials availability:** Data are available via data use agreement, as required by the Columbia University Medical Center Institutional Review Board. All analysis code is available at <https://github.com/elliiothsmith/IEDs>.

**Table 1. Summary statistics for spatiotemporal features of the dataset.**

participant	Seizure Class	N detected IEDs	N (%) traveling waves (LFP)	N traveling waves (MUA)	median speed (cm/s)	Bimodal?	N Seizures
1	recruited	1761	1567 (89.0)	640	20.9	yes	1
2	recruited	1532	1217 (79.4)	131	59.2	no	3
3	recruited	17988	10220 (56.8)	10380	25.3	yes	1
4	recruited	2806	1429 (50.9)	284	63.7	yes	1
5	recruited	2148	1538 (71.6)	1131	108.3	yes	2
6	recruited	3502	3143 (89.7)	2006	69	yes	2
7	penumbral	4348	2132 (49.0)	2236	76.8	yes	5
8	penumbral	8369	7351 (87.8)	4977	134.7	no	0
9	penumbral	834	296 (35.5)	50	80.5	yes	3
10	penumbral	2335	1385 (59.3)	322	70.7	yes	4
<b>Totals</b>		45623	30278	22157			22

# Supplementary Materials:

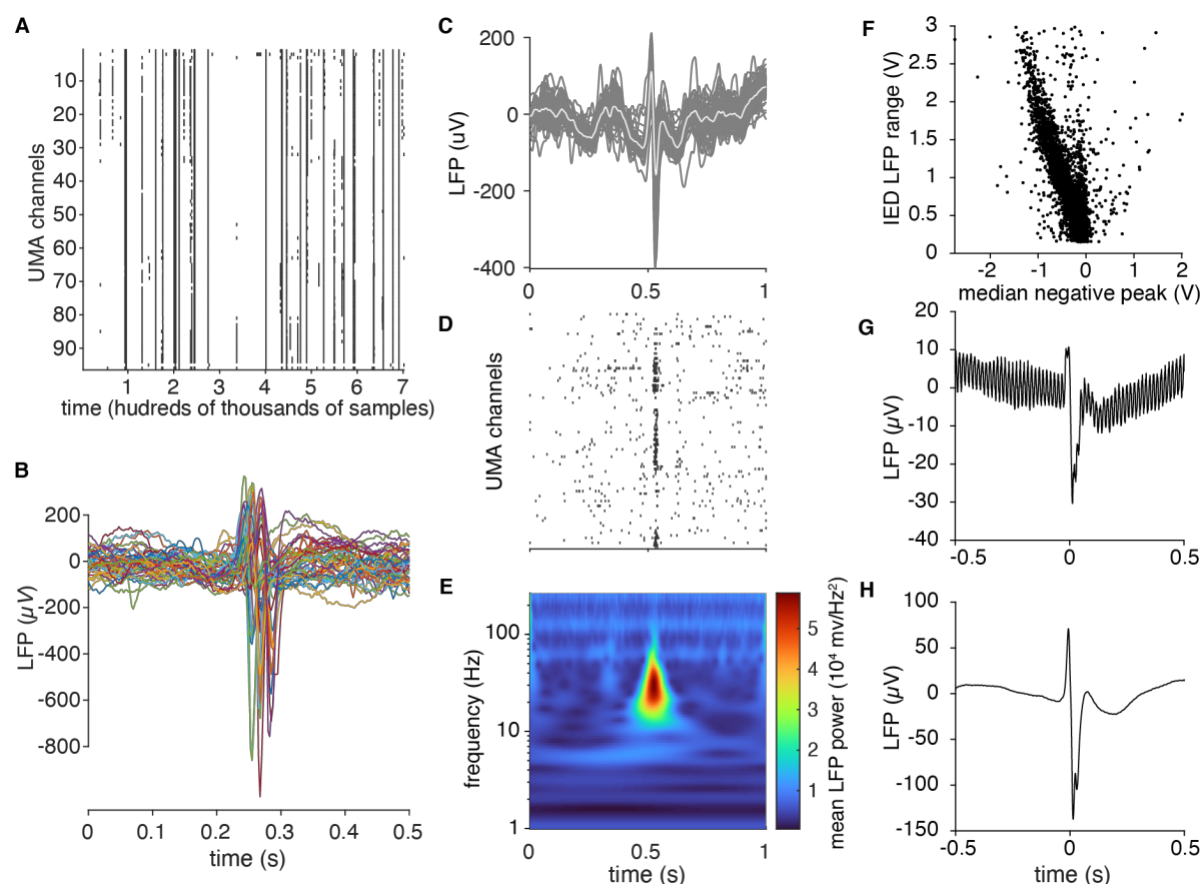


**Figure S1. IED detection and artifact rejection.** (A) Raster plot of IED detection times across UEA channels during a segment of data (approximately half an hour duration). (B) mean IED waveforms for the retained detections shown in (A). These appear as rasters occurring across more than 10 channels in (A). (C) Recordings of a single IED across all microelectrodes. (D) Raster plot of IED-associated MUA firing. (E) Mean spectrogram across microelectrodes for the IED shown in (C). Prominent Beta power, upon which the detection algorithm operated, is clearly visible. (F) A scatter plot of the mean IED negative peak versus the median range of recorded voltages for each IED in one participant after rejecting outliers. (G) Mean IED waveform before amplitude rejection. (H) Mean IED waveform after IED rejection. (G) and (H) show that many large amplitude detections were also highly noisy.

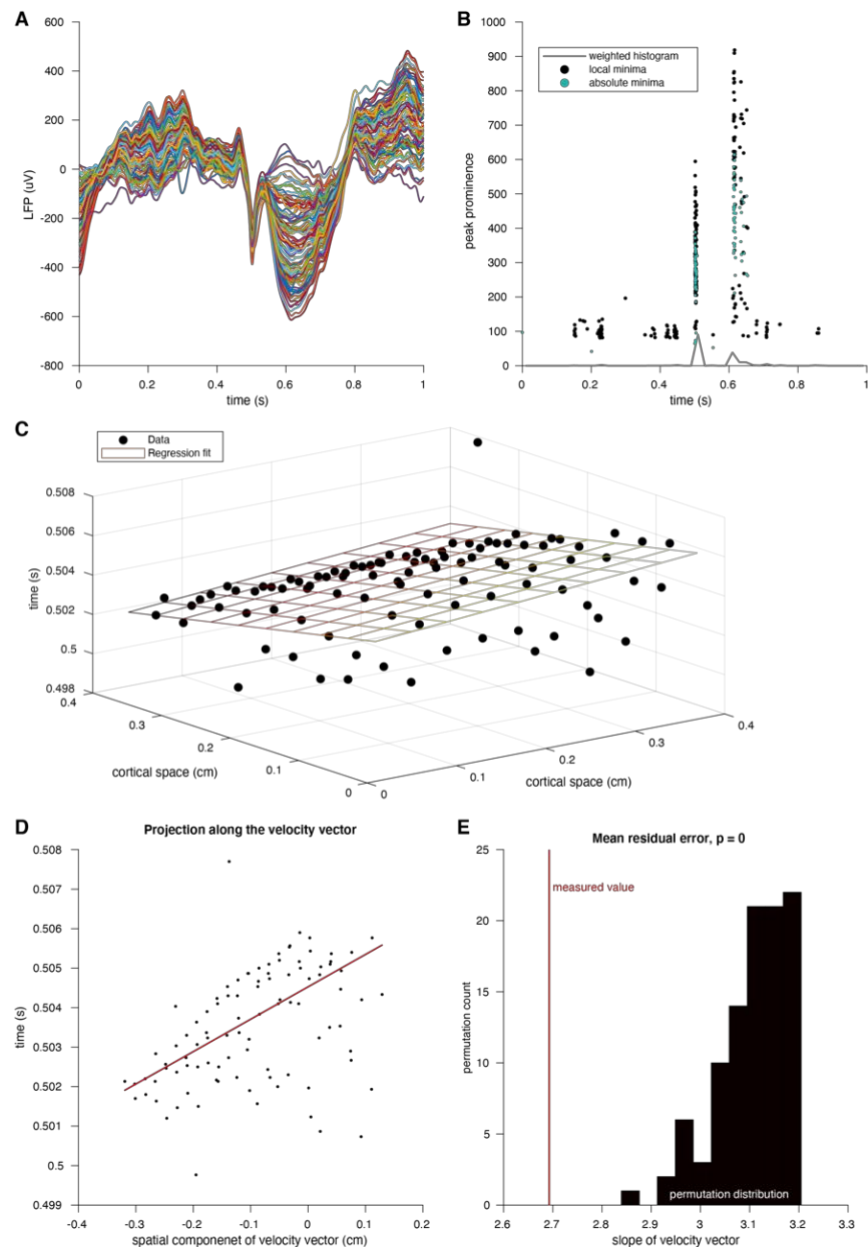


**Figure S2. Classifying IED traveling waves.** (A) Example IED recorded across microelectrodes. Each colored line represents the voltages recorded from a single microelectrode. (B) Scatter plot of IED extrema over time. Black dots show local minima and green dots show absolute minima. The weighted histogram of these points that was used to define the time window used for extrema detection is shown in gray. (C) Three-dimensional scatter plot of voltage minima timings plotted across the spatial footprint of the UEA. The plane from the multilinear regression model, regularized via least absolute deviation, is shown as a grid in spacetime colored by time of occurrence (earlier: black; intermediate: orange; later: yellow). (D) Scatter plot of IED extrema and slope line of the linear regression model projected into two dimensions. (E) Visual representation of the permutation test that was used to operationally define IED traveling waves. The true residual absolute deviation is shown in red and residual absolute deviations from spatially shuffled data are shown in black.

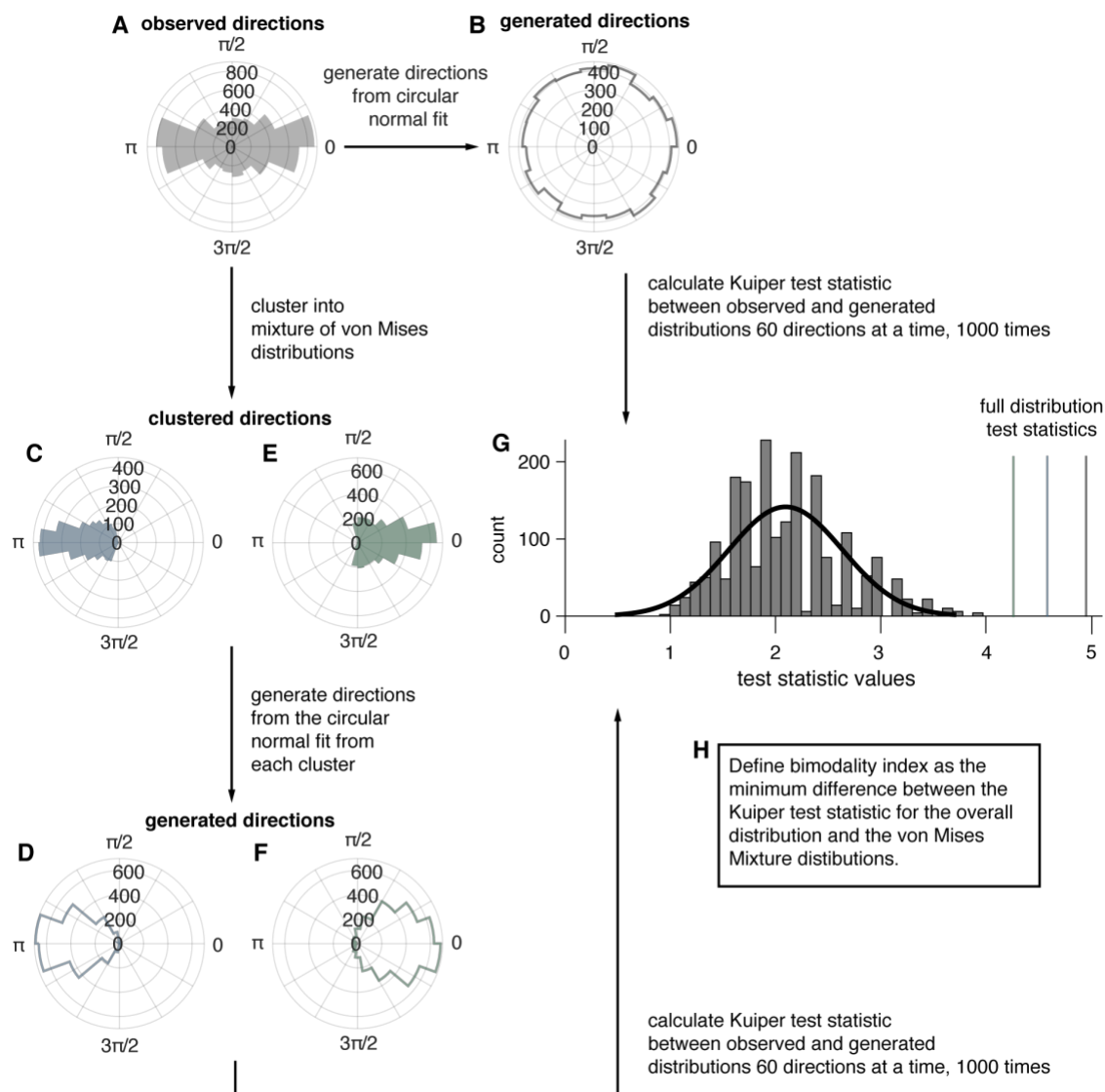


**Figure S3. Procedures for clustering and evaluating the goodness-of-fit of overall and von Mises Mixture distributions.** (A) An example IED distribution for one participant. (B) a distribution of the same number of directions sampled from the circular normal distribution with the same mean direction, and concentration parameter as the distribution in (A). (C) The first clustered distribution of angles from (A). (D) a distribution of the same number of directions sampled from the circular normal distribution with the same mean direction, and concentration parameter as the distribution in (C). (E) The second clustered distribution of angles from (A). (F) a distribution of the same number of directions sampled from the circular normal distribution with the same mean direction, and concentration parameter as the distribution in (C). (G) the permutation distribution of Kuiper test statistics comparing subsamples of angles from real IED distributions and circular normal distributions with the same parameters. The black line shows a gaussian fit to the distribution and colored lines represent the test statistics from the true data distributions. (H) A description of the classification rule for unimodal vs bimodal IED distributions.

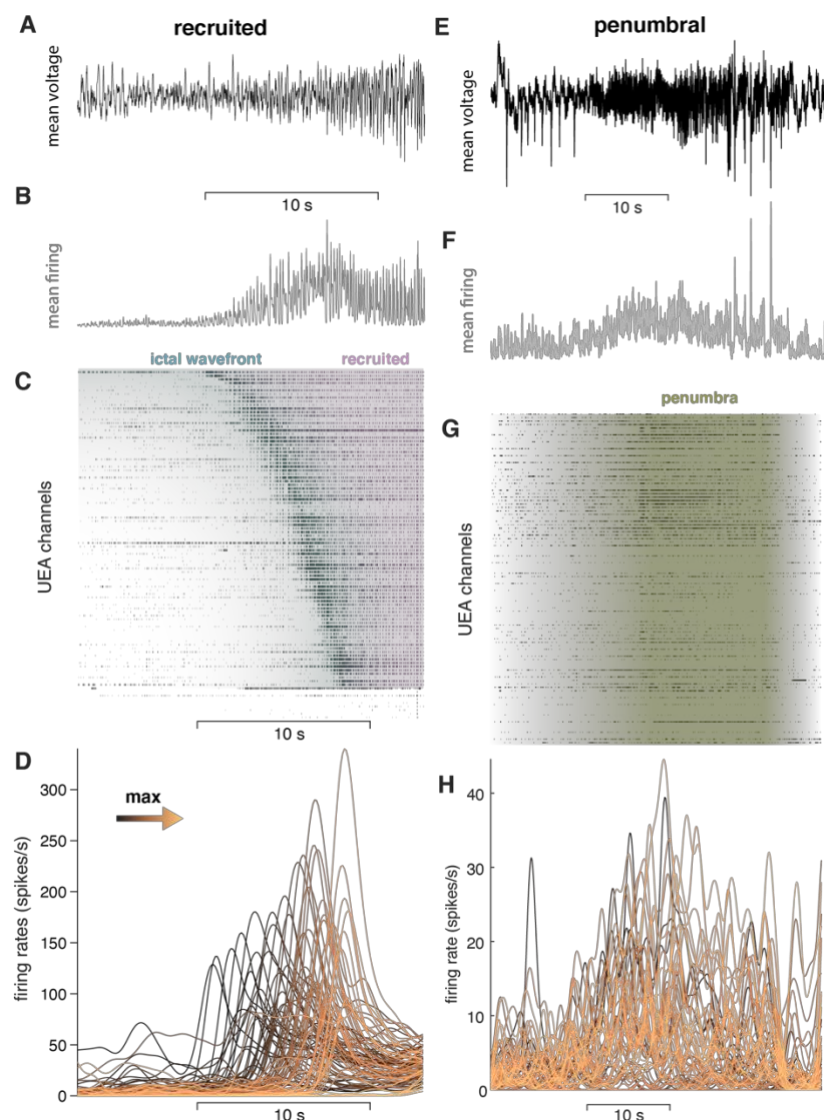


**Figure S4. Examples of each class of microelectrode seizure recording.** (A) Mean LFP around the time of UEA recruitment for the “recruited” category. Scale bar shows 10 s. (B) Mean MUA firing rate across the microelectrodes for the same time period shown in (A). (C) Raster plot of MUA event times for each microelectrode on the UEA sorted by recruitment time. (D) MUA firing rates on each microelectrode colored by order of recruitment from black to copper. (E) Mean LFP for a seizure in the “penumbral” category. Scale bar shows 10 s. (F) Mean MUA firing rate across microelectrodes for the same time period shown in (E). (G) Raster plot of multiunit event times for each microelectrode. (H) Multiunit firing rates for each microelectrode colored by the timing of maximal firing during the seizure window. Note the lack of spatiotemporal organization in the “penumbral” example.

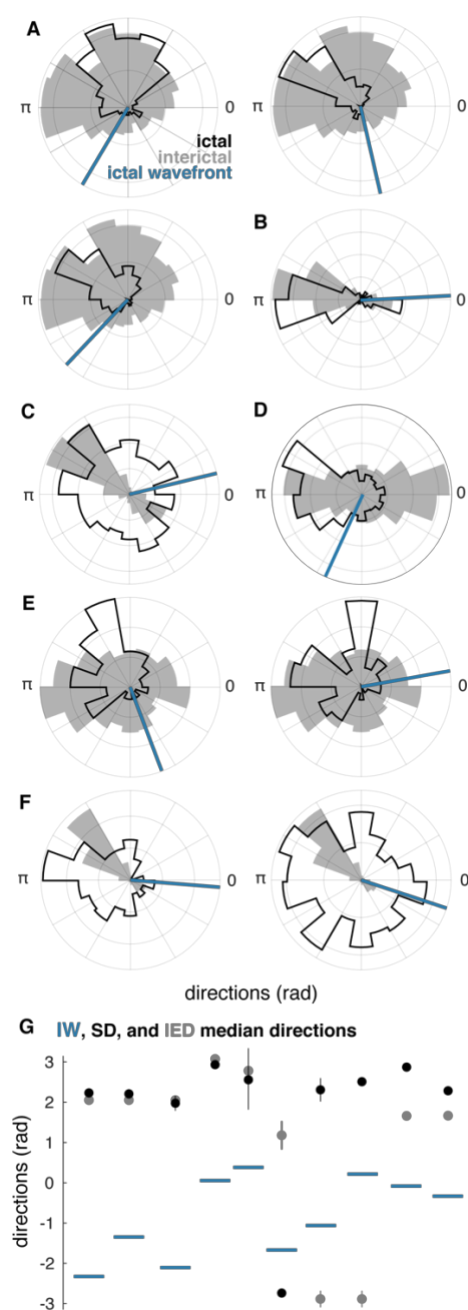


**Fig. S5. Raw IED and SD distributions in “recruited” UEA recordings.** (A-F) Each lettered subpanel corresponds to one participant. Each polar histogram corresponds to one seizure. Gray histograms show IED distributions. Black histograms show SD distributions, and blue lines show the directions of IWs. (G) direction summaries for each seizure ordered and color coded as in (A-F). Dots indicate median directions and lines indicate standard deviations.

# Algorithm S1. Algorithm for detecting IEDs from microelectrode recordings.

**Input:** A matrix of microelectrode voltage recordings,  $V(c, t)$ , where measured voltage is a function of time,  $t$ , and which microelectrode array channel it was recorded on,  $c$ .

**Output:** A vector of IED times,  $I(t)$ .

- 1: **for** each  $c$ , do:
- 2:     filter data between 20 and 40 Hz (non-causal, 4th order Butterworth filter)
- 3:     detect peaks,  $p$ , in filtered signal greater than 8 times the standard deviation of the beta power in the data.
- 4:     discard peaks that occur within 250 ms of a preceding detection
- 5:     **for** each  $p$ , co-occurring within 250 ms, across more than 10 microelectrodes.
- 6:     find all local minima of  $V(c, t)$  in time, across all  $c$ .
- 7:     bin local minima in time, across all  $c$ .
- 8:     convolve the resulting histogram with a modified Heaviside function,

$$H(t): \begin{cases} 0, & 0 \geq n < 0.4 \\ 10t, & 0.4 \geq n < 0.5 \\ -t, & 0.5 \geq n < 1 \end{cases}$$

- 9:     find absolute minima of  $V(c, t)$  within the bin containing the most local minima.

**Table S1. Clinical details for research participants.**

<b>Participant</b>	<b>Age</b>	<b>sex</b>	<b>Epileptogenic zone</b>	<b>UEA implant site</b>	<b>Pathology</b>	<b>Outcome</b>
<b>1</b>	30	male	right lateral and mesial temporal lobe; nonlesional	Right middle temporal gyrus, 4 cm posterior to the temporal pole	Mesial temporal sclerosis	Engel 2 at 22 months
<b>2</b>	25	male	Left mesial temporal lobe	Left middle temporal gyrus, 3 cm posterior to temporal pole	Non-specific	Engel 1a at 7 months
<b>3</b>	32	male	Right mesial temporal lobe	right inferior frontal gyrus	Normal hippocampus	Engel 1a at 2.5 years
<b>4</b>	30	male	left supplementary motor area	left supplementary motor area	N/A (multiple subpial transections performed)	Engel 3 at >2 years
<b>5</b>	39	male	left frontal operculum	left lateral frontal, 2 cm superior to Broca's Area	Nonspecific	Engel 1a at >2 years
<b>6</b>	32	female	left inferior temporal lobe	inferior temporal gyrus, 2.5 cm from temporal pole	1 neuronal loss; lateral temporal nonspecific	Engel 1a at 55 months
<b>7</b>	19	female	right posterior lateral temporal	Right posterior temporal, 1 cm inferior to angular gyrus	Non-specific	Engel 1a at >2 years
<b>8</b>	28	male	left dorsal posterior prefrontal cortex	left posterior middle frontal gyrus	Mild reactive astrogliosis, patchy microgliosis, Chaslin's marginal sclerosis	Engel 3a at 32 months
<b>9</b>	26	male	left middle subtemporal	left posterior inferior temporal gyrus	Diffusely infiltrating low grade glioma, IDH-1 negative	Engel 4a at 2 years, 5 months
<b>10</b>	30	male	right middle inferior temporal gyrus	right middle temporal gyrus	Mild astrocytosis	Engel 1a at 12 months

**Movie S1. Video of IEDs and ictal recruitment.** A movie showing several pre-ictal IEDs propagating in the opposite direction of seizure expansion, in the same direction as SDs. The top trace shows the mean LFP across all microelectrodes for the beginning of one seizure. The lower three panels show three types of data superimposed across the footprint of the microelectrode array. The lower left panel shows LFP voltages recorded on each microelectrode. The lower middle panel shows the slow multiunit firing dynamics, in which the slow propagation of the ictal wavefront can be observed. The lower right panel shows the fast multiunit firing dynamics. The movie progresses at 1/8<sup>th</sup> the speed of real time and the red bar shows the passage of time, with three seconds indicated by the temporal scale bar.